Babes-Bolyai University
Faculty of Physics

Doctoral thesis summary

Development of new unconventional methods for the fabrication and characterization of sensing platforms based on graphene derivatives

by

Diana Zaharie-Butucel

Scientific Advisor

Prof. dr. Simion Aştilean

CLUJ-NAPOCA

2017

Table of contents

Outline

What started as a simple poster on the hallways of the Physics Faculty in Cluj-Napoca became the subject of my daily inquiries for the last three years. In my preparatory stages of a researcher' career I played with plasma physics particularly plasma in contact with liquids. With a desire to pursue a PhD, in the weeks concluding the master program, I was at a crossroads. A not so much explored avenue, which could have been a great subject, was dealing with nano and micro-particle synthesis assisted by plasma. However, forced by circumstances (that year there were no available doctoral positions at the plasma department) I applied for a PhD in a different group and was about to work with graphene. My only encounter that far with graphene, was with the shadowy poster featuring the 2010 Nobel prize award. As I began studying, it became clear that in the timeframe following the isolation of graphene, the research somehow channeled towards this new exciting material and in ten years most of the fundamental issues were settled. The challenge was to find cost-effective ways to produce graphene and ensure that the developed applications are competitive on the large-scale compared to other recognized materials.

The ultimate goal of the research detailed in this thesis is to provide simple tools for the design and fabrication of chemically converted graphene platforms facilitating the development of applications which could in turn enable the transfer from the lab level to the technological scale. To this end, on one hand I employed a cost-effective technique to fabricate regular arrays of chemically converted graphene films which is a simplified alternative to the well-established yet complicated protocol of patterning graphene. On the other hand, addressing the need for elucidating the structural changes when designing graphene/moiety platforms I developed a dual Raman and two-photon excited fluorescence lifetime imaging analysis which proves to be a visual tool for the distribution of moieties on the graphene lattice.

My thesis is structured in three main sections. ***Part I. Review of related literature and theoretical aspects*** is the result of my outside-the-lab effort to understand graphene and consists of several theoretical aspects regarding graphene and related literature relevant to the context of the. The results of my research on the fabrication and evaluation of graphene oxide and chemically converted graphene films/interfaces with a view to developing resistive or optical sensors for technological and biological applications is presented in ***Part II***. The Appendices are added in ***Part III*** of the thesis.

Chapter 1. Overview of graphene settles the historical background of graphene and clearly defines its distinctive properties ensuing from the two-dimensional honeycomb structure. Out of the two most widespread methods for the large-scale production, a special section is dedicated to the chemically converted graphene, which is the basic material used in this thesis.

In **Chapter 2. Evaluating the properties of graphene**, I focus on understanding the basic carrier transport mechanisms in pristine graphene and chemically converted graphene flakes and the optical absorption and emission occurring in these materials. Special attention is given to the Raman emission which is easily discernible in carbon structures

and provides invaluable information. All of these are relevant to how the potential of graphene can be used in sensing devices.

Moving to ***Part II*** and the most important part of my thesis presenting my research results, **Chapter 3. Optimization of the production method** is an essential part in which I validate by spectroscopic and microscopic means the chosen synthesis method and produce graphene oxide and chemically converted graphene dispersed in water for further processing into films.

In **Chapter 4. Convective self-assembly (CSA) of chemically converted graphene: a route towards flexible transparent electronic devices** I employ CSA for the fabrication of patterned and continuous CCG films with well-defined geometry and demonstrate its superiority to other techniques used in literature, in terms of cost-effectiveness, simplicity, material-loss and operating conditions. Expanded on in the rest of the chapter and a step further to the large scale application of graphene, is the design of multivalent resistive sensors for strain and humidity with CCG films assembled by CSA.

Chapter 5. Revealing the structure and functionality of graphene oxide(GO) and reduced graphene oxide(rGO)/pyrene carboxylic acid (PCA) interfaces by correlative spectral and imaging analysis is devoted to the dual Raman and two-photon excited fluorescence lifetime imaging tool developed for the analysis of graphene/moiety interfaces applied on GO-PCA and rGO-PCA. Promising results on the anchoring recognizing moieties-aptamers on these type of materials pave the way for the development of biosensors.

Chapter 6 offers a summary of the conclusions and perspectives offered by the work done in this thesis.

In ***Appendices***, a more in-depth presentation of several theoretical aspects is given together with supplementary measurements performed throughout the studies and a list of personal publications which contributed to the dissemination of my work.

Keywords*: graphene, convective self-assembly, flexible electronics, raman, two-photon fluorescence*

Part I – Review of related literature and theoretical aspects

Chapter 1. Overview of graphene

1.1 History

Long theorized by the condensed-matter physicists, graphene is said to have revolutionized science, when in 2004 researchers from Manchester isolated the elusive two-dimensional carbon sheet and reported the electrical field effect [1]. In the last ten years of research, despite the sustained efforts of both the public and private organizations, commercially available products are still rare [2]. One of the voiced concerns is still the high price required for graphene production [2]. In the end, the current standing of graphene is researching for more cost-effective production ways and still lacking a commercial launcher app [3].

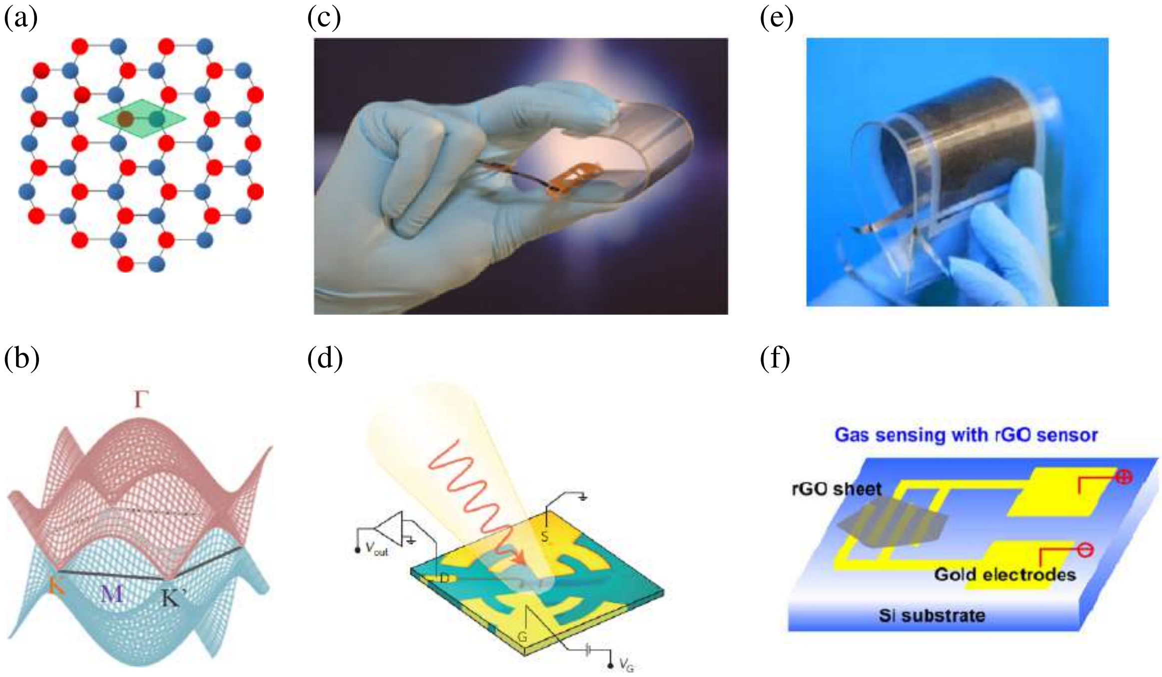

Figure 1.1- (a) Graphene crystal lattice and primitive cell comprising two types of carbon atoms A (red) and B (blue); (b) Band structure of graphene containing the π and π* bands intersecting at the corners of the first Brillouin zone; (c) flexible multi-touch screen based on graphene [4]; (d)antenna-like graphene based THz photodetector [5]; (e) Li-ion graphene foam battery [6]; (f) gas sensor with graphene FET [7].

1.2 Graphene. Structure and properties

The unique properties of graphene stem from its atomic arrangement into a one-atom-thick honeycomb lattice of carbon atoms. The planar σ-bonds endow graphene with exceptional mechanical properties (tensile strength of 130 GPa [8], Young modulus of 0.5 TPa [9]) and high thermal conductivity 5000 W m^{-1} K^{-1}. The electronic dispersion of graphene modualates the optical and electronic properties. Graphene is highly transparent and has a universal absorbance ~2.29%, for energies larger than the Fermi level [10]. Electrically, graphene is a semiconductor with band-gap zero and the carriers can reach mobilities as high 200 000 $cm^2 V^{-1} s^{-1}$ in suspended graphene [11]. Furthermore, it posseses enhanced surface area 2630 m^2g^{-1} open for different types of chemical interactions [12].

Now that the predicted characteristics of graphene are up for grabs the opportunities of harnessing them are close to amazing. The ideas of affordable flexible and robust electronics, terahertz devices, broadband photodetectors or highly sensitive biosensors are just some of the attractive possibilities.

1.3 Production methods

Apart from mechanical cleavage or the „scotch-tape” method two main methods gained popularity in the scientific community: chemical vapour deposition (CVD) and liquid phase-exfoliation. Ultimately, one should find a compromise among the desired application, required quality and size of graphene, without omitting the cost factor as evident from table 1.1 [13].

Table 1.1 – Methods for large-area production of graphene, the resulting properties and possible applications. Adapted from Novoselov *et al* [13].

Method	Crystallite size (µm)	Sample size (mm)	Carrier mobility (at room-temperature) ($cm^2 V^{-1}s^{-1}$)	Applications
Mechanical exfoliation	>1000	>1	$>2 \times 10^5$	research
Chemical exfoliation via graphene oxide	~100	Infinite as layer of overlapping flakes	1	Coatings, paint/ink, composites, transparent conductive layers, energy storage, bioapplication
CVD	1000	~1000	10000	Photonics, nanoelectronics, transparent conductive layers, sensors, bioapplications

Chapter 2. Evaluating the properties of graphene

The following chapter is dedicated to a brief insight into the properties of graphene relevant to this thesis together with theoretical and practical aspects on how to evaluate them. A particular interest is given to the carrier transport inside graphene, the optical absorption and emission and finally to the Raman response of graphene and related materials. Equally important and discussed below, are the capacities of graphene which recommend it for sensing and the performances they reached so far in workable devices.

2.1 Carbon structures as seen by Raman spectroscopy

In the case of graphene, Raman spectroscopy is one of the most widely used techniques for probing various properties of graphene, such as number of layers and stacking geometry, edge chirality, amount of doping, defect density, structural damage, functional groups, thermal properties and even strain [14].

2.2 The sensing capacity of graphene

Strain sensing with graphene

Out of the many applications, what makes graphene appropriate for strain sensors is the electrical mechanical coupling observed both in suspended monolayer graphene and different configurations of chemically converted graphene (CCG) [15]. The sensitivity of a strain sensor is termed the gauge factor and can be defined as [16]:

$$\mathrm{g} = \frac{\Delta A}{A_0} / \varepsilon$$

where A_0 is the electrical property measured at rest and ε the strain induced.

Humidity sensing with graphene

The basic principle for humidity sensing on graphene is related to the modulation of the electrical properties by physical adsorbtion of water molecules [17].

Photodetection with graphene

In graphene, the zero-band gap enabling carrier generation on a broad range energy spectrum, the wavelength independent absorption, the high carrier mobility and the tunable Fermi level by doping [5] ensure all the requirements for effective photodetection.

Part II- Research results and discussions

Chapter 3. Optimization of the production method

When trying to develop a graphene based application, the production method is essential both in terms of the quality required and the costs. In this chapter, we explore two production methods: (i) a new technique assisted by plasma in contact with water chromophore solutions and (ii) a wide-spread top-down technique based on the oxidation of graphite. We opted for using top-down approaches, trying to maintain the production costs at a minimum.

3.1 New synthesis methods- atmospheric plasma in contact with liquid

The procedure for the synthesis is simple: a solution of methylene blue (MB) (25 ml, 100 mg l^{-1}), undergoes plasma treatment for a time frame of solely tens of minutes. The plasma discharge, generated inside bubbles in the dye solution, has a degradation effect and concurrently carbon structures are formed. For this study two plasma gases were used namely argon (Ar) and helium (He) at extremely low flow rates (0.35 l min^{-1}).

Morphology of the carbon structures

The TEM images (figure 3.1) of the MB solutions treated under plasma at different time intervals offer information related to the morphology of the carbon structures obtained. The resulting structures are polydisperse in size and their shape varies among spherical, irregular and even sheet-like presenting as a uniform thin layer.

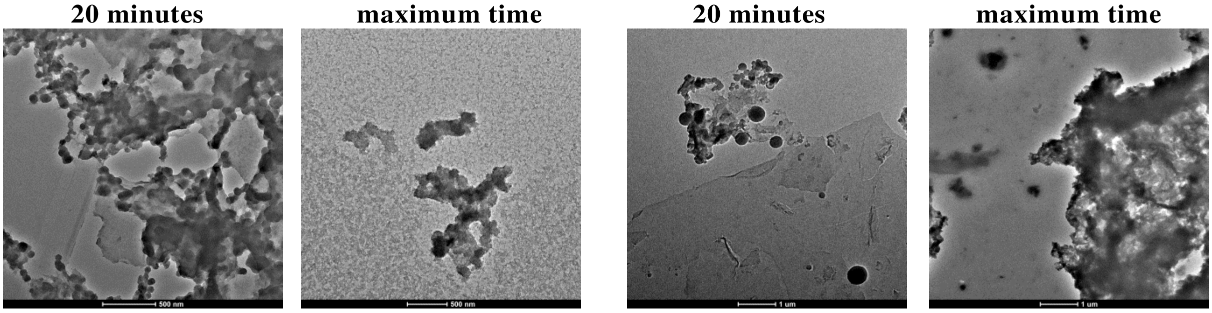
20 minutes **maximum time** **20 minutes** **maximum time**

Figure 3.1 - TEM images of the Ar plasma carbon structures (left) and of He plasma carbon structures (right) obtained at 20 minutes and maximum time treatment.

Based on the TEM images we assume that there are two simultaneous processes: the formation of the particles from the MB molecules and the degradation of the particles by the plasma which produces a varied morphology and dimensions for the particles. The Ar plasma leads to nanoparticles with lower polydispersity and the He plasma leads to the formation of microparticles with increased polydispersity.

Amorphization and crystallinity of the carbon structures

Raman spectroscopy is the most straightforward tool in evaluating the level of disorder in carbon structures and can help discriminate among them.

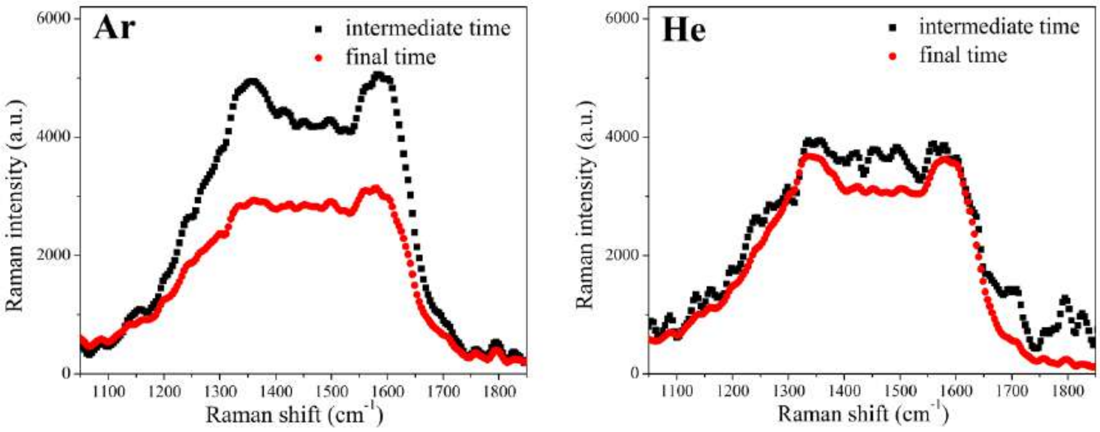

Figure 3.2 - Raman spectra of the particles obtained with Ar plasma (left) and He plasma (right) at 20 minutes and the maximum time treatment.

For both the studied gases, the carbon structures are between nanocrystalline graphite and low sp^3 amorphous carbon in nature, presenting wide overlapping ***D*** and ***G*** peaks with I_D/I_G peak ratios comparable to 1 (see figure 3.2). The difference however is that as the time treatment increases, the Ar plasma has a destructive effect on the particles (the peaks widen even more and are less distinctive) whilst the He plasma appears to induce a certain ordering in the resulting structures (the peaks become more well defined). The plasma assisted synthesis leads to a plethora of carbon structures differing both in morphology and crystallinity. To produce graphene, additional separation and purification procedures are required, consequently this approach was not explored any further.

3.2 Development of established protocol- CCG synthesis via modified Hummers method

The second approach for the graphene synthesis is based on the widely utilized Hummers protocol for graphite oxide synthesis [18]. GO is produced by exfoliating graphite oxide to single layered and few layered in ultrasound bath. Finally to produce clean CCG flakes, the GO is chemically reduced with HH under microwave radiation in an Anton Paar Monowave 300 system [19]. No additional surfactants are needed to stabilize the resulting CCG suspension.

Spectroscopic validation

The **UV-vis absorption spectrum** of GO in water (figure 3.3) presents the typical main band centered at 230 nm corresponding to a π→π* transition C=C in amorphous carbon systems and the shoulder around 300 nm assigned to a n→π* transition of the C=O bonds [20].

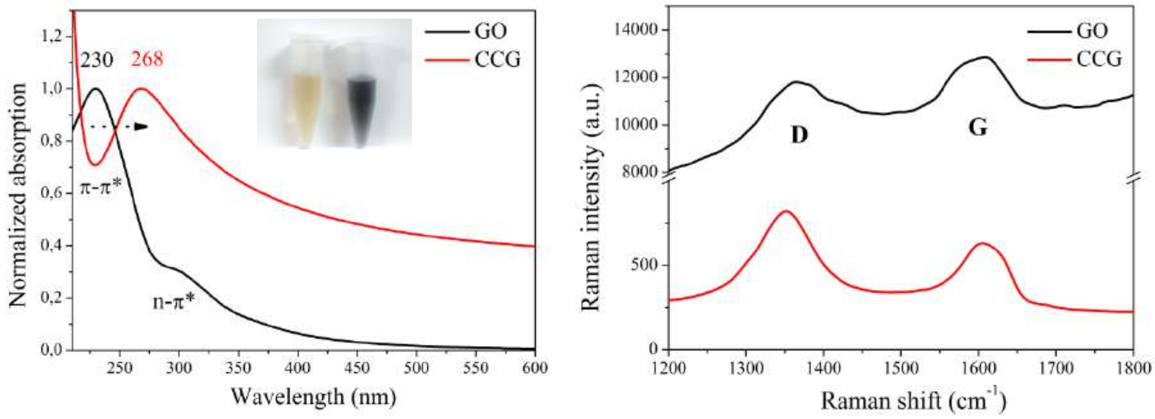

Figure 3.3 – (left) UV-vis absorption spectra of GO (black) and CCG (red) in water. The inset is a picture of GO (yellow) and CCG (dark) flakes in water; (right) Raman spectra of GO (black) and CCG (red) suspensions in water

After the chemical reduction process assisted by microwave radiation, the main band has a red shift, the shoulder is no longer visible and the absorption increases throughout the entire visible and NIR range. All these changes are consistent with a restoration of the sp^2 network by the partial removal of oxygen and the conversion of the sp^3 sites to sp^2.

Raman spectra of GO and CCG aqueous suspensions (figure 3.3), depict the ***G*** and ***D*** peaks characteristic to carbon structures. Following the reduction process the peaks width become narrower and the I_D/I_G ratio increases. These changes are in agreement with previous studies, which suggest that the reduction facilitates the conversion of the sp^3 sites to sp^2 ones. The sp^2 domains do not increase in size but rather new isolated ones are formed and the defects introduced inside the basal plane during the graphene oxide synthesis still remain increasing the I_D/I_G ratio [21]. Thus the resulting CCG has a restored sp^2 conjugation which is expected to improve the electrical and optical properties compared to GO.

Microscopic characterization

AFM is useful in estimating the number of layers in graphene and validating the exfoliation of graphene materials using graphite as starting material. The reported values for single-layer graphene ranged from 0.4 to 1.7 nm [22,23]. As seen in figure 3.4, the resulting GO consists of micrometer sized flakes mainly single layered. After reduction, the removal of oxygen groups the decrease the thickness of the CCG layer. TEM images confirm the monolayer character of both GO and CCG (figure 3.4).

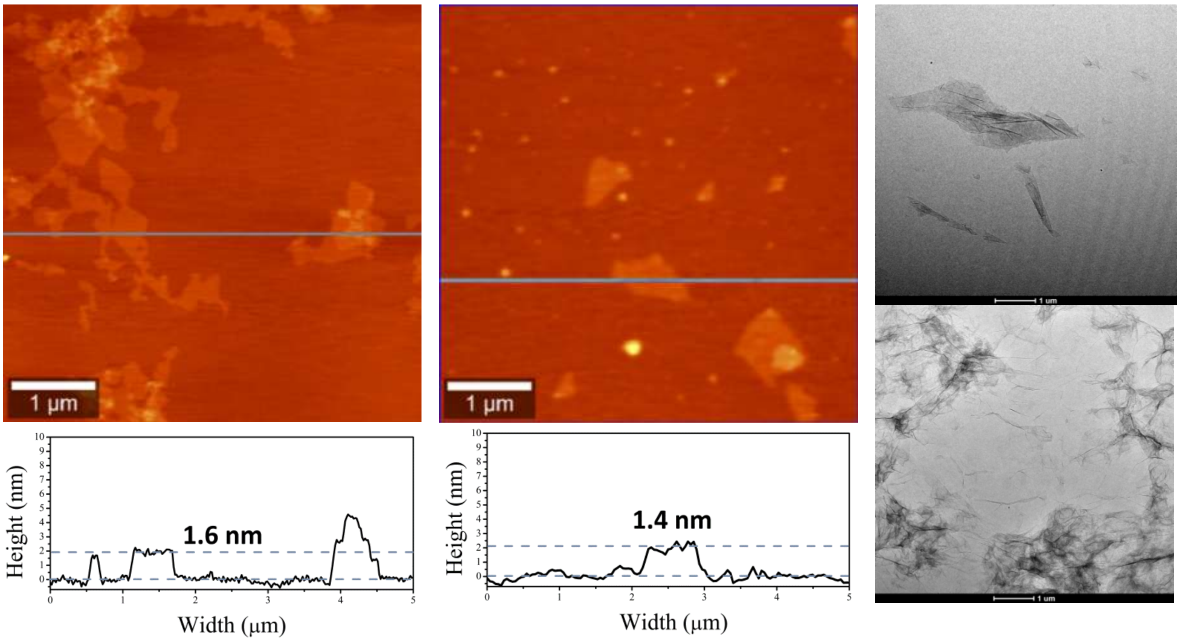

Figure 3.4 – AFM topography images of GO (left) and CCG (middle) and the corresponding cross-sections; (right) TEM images of GO (top) and CCG (bottom).

Conclusions

- Plasma in contact with liquid has a low yield for the production of graphene and further processing and separation techniques are required to improve the yield.
- Optimizing a modified well-known protocol, delivers GO and clean CCG with well defined lateral size, dispersed in liquid phase in an extremely cost-effective manner.
- The quality of GO and CCG is validated by spectroscopic and microscopic techniques.
- The GO and CCG materials can be readily used as is or further modified with molecules as required.

Chapter 4. Convective self-assembly of chemically converted graphene: a route towards flexible transparent electronic devices

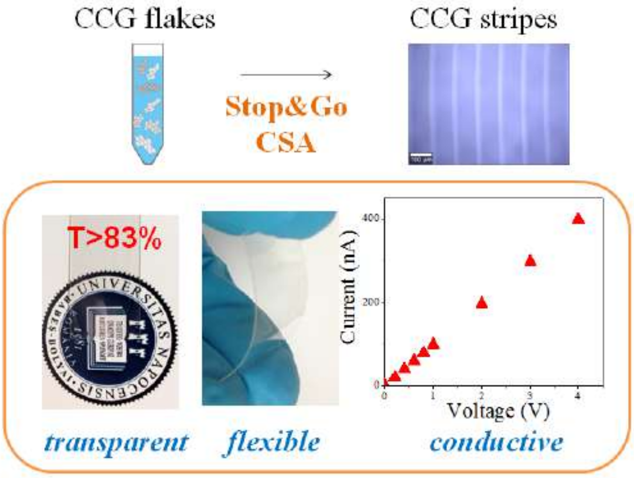

Convective self-assembly of chemically converted graphene. Efficient and cost-effecttive route for the development of flexible electronic devices

Chemically converted graphene (CCG) currently represents an attractive alternative material for graphene and its already well-known electronics applications. Due to its liquid phase processing it can be produced inexpensively on large scale, but its deposition into films/patterns of defined geometry on solid substrates remains challenging. In this chapter, CCG micro-stripes/wires with controlled morphology are prepared on flexible and rigid substrates by Stop&Go Convective Self-Assembly. This method allows the deposition of regular arrays of CCG stripes by independently adjusting the stripe geometry and array period in an inexpensive, clean and fast way, and without any lithographic patterning. The as-obtained CCG stripes are highly transparent, flexible and good electrical conductors, properties which are of great value for future electronic devices. We investigate and harness their multivalent potential in electronics applications, with a focus on sensing particularly fabricating sensors which are optically transparent.

CCG micro-stripes were fabricated using *Stop&Go* Convective Self-Assembly (*Stop&Go* CSA) [24] on flexible substrates (175 µm thick polyethylene terephthalate (PET) foils, 50 µm thick polyimide foils (PID)) and rigid substrates (glass slide, Si/SiO_2 wafers). The customized CSA setup consists of a supporting glass slide placed at a small angle (20-25°) in the proximity of a substrate (~200 µm distance). A droplet of aqueous suspension of CCG flakes (0.05 mg ml^{-1}) was pipetted in the cusp between the glass slide and the substrate to form a linear meniscus that is horizontally translated across the moving substrate.

4.1 CCG stripes of controlled morphology

A schematic representation of the deposition process of CCG flakes by *Stop&Go* CSA is presented in figure 4.1 By adjusting several of the parameters in the *Stop&Go* CSA protocol, the width and the period of the stripes could be controlled independently. Specifically, two parameters (t_{stop} and D) were modified in the following way: when one was varied the other was constant. While the setup and protocol allow the modification of these parameters in a wide range of values, only a representative selection is presented in figures 4.2 and 4.3.

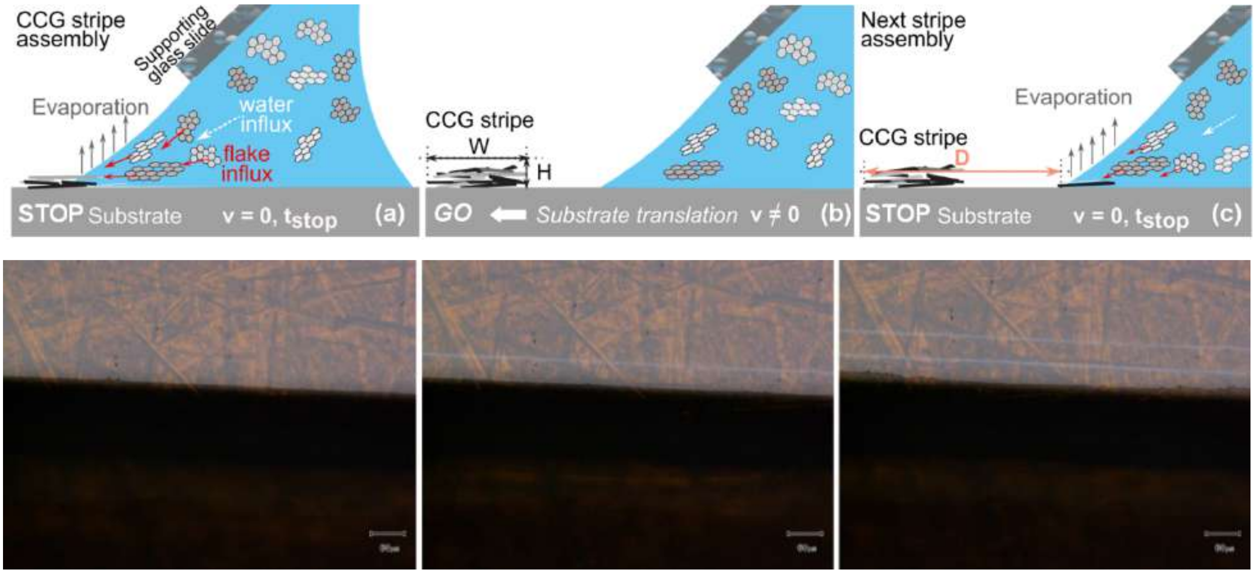

Figure 4.1 - Schematic representation of CCG flake deposition on PET substrates by *Stop&Go* CSA. (a)STOP stage: the contact line is maintained at the same position for a time interval t_{stop} and due to evaporation at the meniscus level, the CCG flakes adhere to the substrate; the evaporation flux causes flake and water fluxes toward the contact line, which provide a steady supply for the assembly of CCG flakes along the contact line (b) GO stage: the substrate is translated at a constant speed *v*, across a distance D; *v* is high-enough so that only low evaporation occurs and there is virtually no assembly at the contact line (c) STOP stage is repeated and a new assembly process starts. In the second row the corresponding optical images (10× magnification) taken during the assembly are presented.

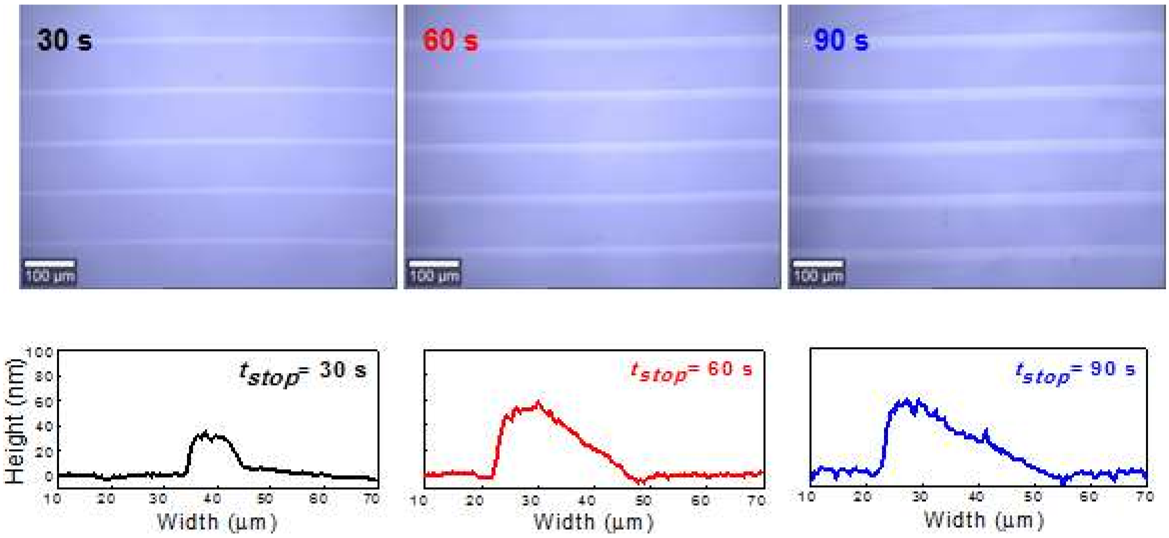

Figure 4.2 - Optical microscopy images and corresponding AFM cross sections for CCG stripes on PET substrates obtained with t_{stop}: 30, 60 and 90 seconds (D=100 µm).

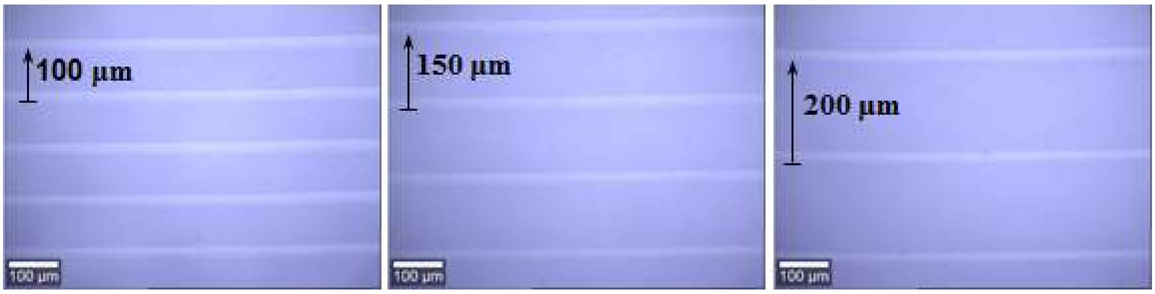

Figure 4.3 - Optical microscopy images of CCG stripes on PET substrates obtained with period *D*: 100, 150 and 200 µm (t_{stop}=60 seconds).

Different morphologies could be envisioned by multidirectional successive assemblies such as grids [25]. Last but not least, because of the CSA compatibility with a variety of colloids it implies that one could easily fabricate complex patterned films combining different types of materials. Some preliminary results towards these goals are presented in figure 4.4.

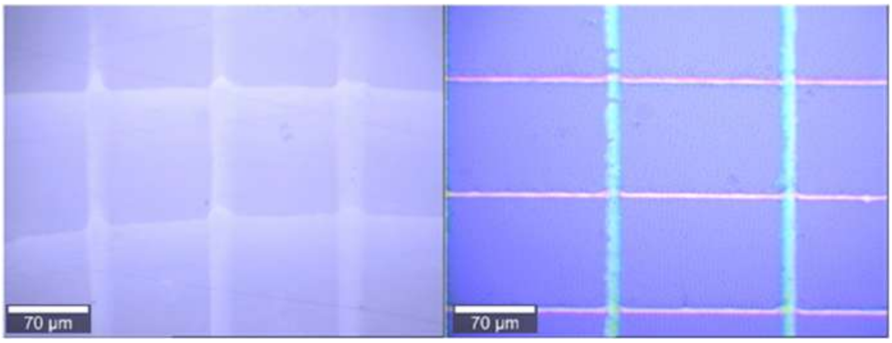

Figure 4.4 - Optical microscopy image of CCG grid on PET substrate (left) and combined Au nanoparticles and CCG stripes on Si/SiO_2 (right).

A closer examination of the surface morphology of the CCG stripes was made by SEM. A representative SEM image is presented in figure 4.5 and shows that the CCG stripe surface is wrinkled, consistent with the AFM measurements. The folding and the rippling occur due to the physical confinement of the CCG flakes in the meniscus region during the solvent evaporation.

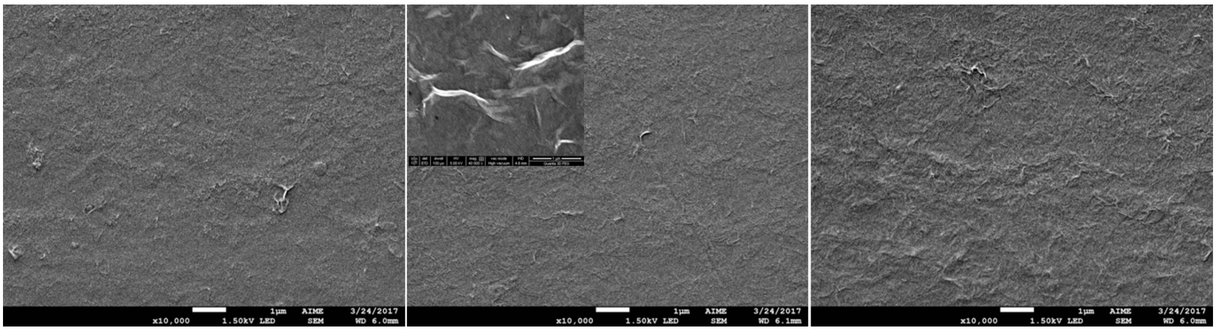

Figure 4.5 - SEM image of CCG stripes on PET substrate (t_{stop}=30, 60, 90 s). The inset represents a zoom in image of the 60 s CCG stripe showing an enhanced view of the folds and ripples.

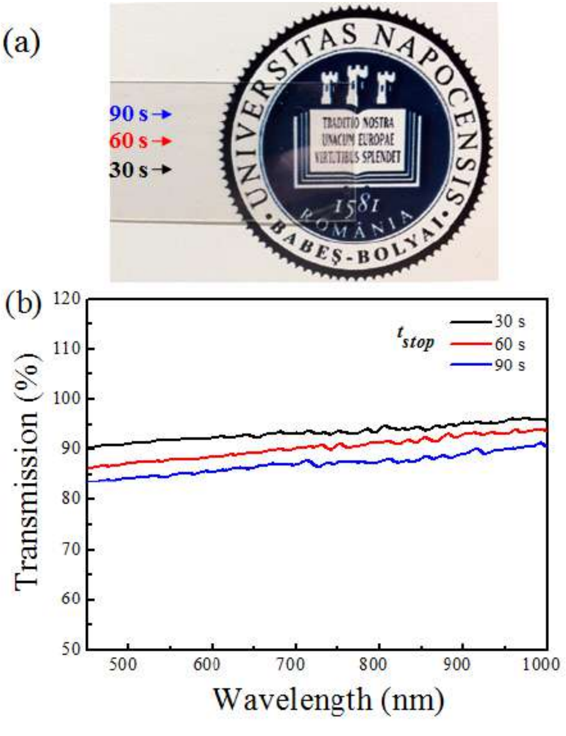

Figure 4.6 - (a) Picture of three sets CCG stripes on PET obtained with t_{stop} (30, 60 and 90 s) and *D* (100 µm) constant; **(b)** Transmission spectra for the CCG stripes on PET substrate obtained by varying t_{stop} (30, 60, 90 s) and D (100 µm) constant.

Optical transmission

It is straightforward to assess the excellent transmission properties of the CCG stripes from the photograph in figure 4.6(a), in which the logo is clearly visible through the CCG stripes on PET. The optical transmission of the CCG stripes including the thickest ones, has averaged values over 85% across the entire 450-1000 nm interval(figure 4.6(b)) which are to our knowledge among the highest observed for graphene films obtained from flakes suspension.

Electrical properties of CCG self-assembled stripes

The electrical performance of the CCG stripes is essential when trying to produce applications related to electronics and optoelectronics which is why it is relevant to characterize the electrical behavior in the low/high field, to estimate the carrier mobility and understand how the transport occurs inside the assembled stripes.

Low field regime

The I-V characteristic of the CCG stripes (figure 4.7) is indicative of a metallic behavior similar to a resistor, at least in the tested interval. There is a linear dependence of the current regardless of the voltage sweeping direction and no hysteresis effects occur. The estimated resistivity of CCG stripes is of the order $10^{-2}\Omega.m$, several orders greater than graphite suggesting that the electron transport is different in the two cases, which is expected. In pristine graphene, in which the sp^2 lattice is perfect, the electrons move freely whereas in CCG monolayers the free movement of electrons is impeded by the intercalation of defects and disorder domains among the sp^2 ordered clusters.

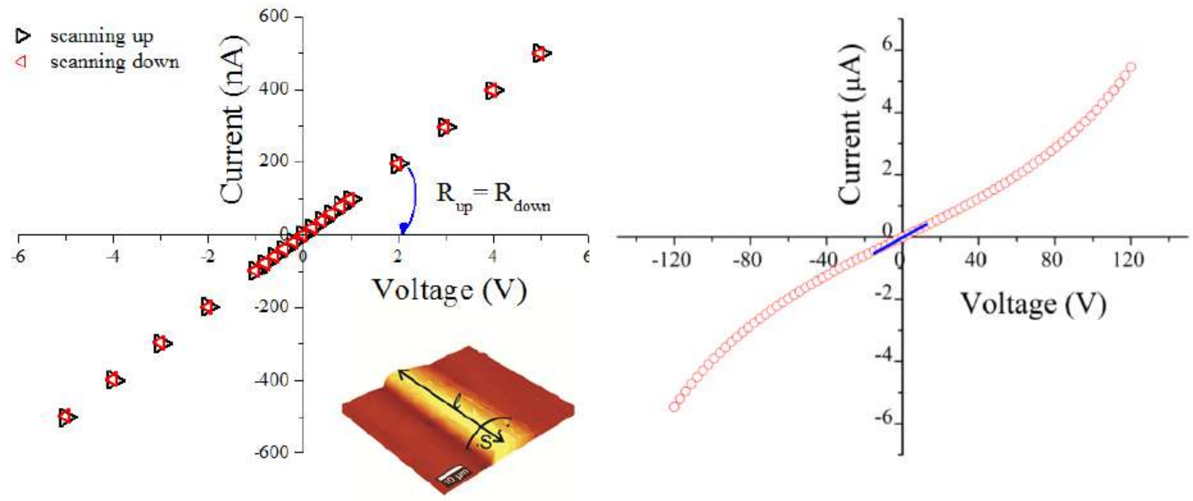

Figure 4.7 - (left) Plot of current versus voltage by sweeping the voltage in the [-5V, 5V] interval for 25 CCG stripes on PET (t_{stop} = 60 s, D = 100 µm). The inset is a representative AFM image of the CCG stripes ;(right) Non-linear current-voltage characteristic of CCG stripes (FL-CCG) on PET in the high-field regime obtained by sweeping the voltage in the [-120 V, 120V] interval; the length of the CCG channel was ~50 µm..

High field regime

The current-voltage characteristics of the CCG stripes in the high field regime, is presented in figure 4.7. The electrical behavior of the self-assembled stripes in the non-Ohmic regime is similar to the one of disordered semiconductors. Even at low voltages the stripes conduct electricity suggesting that percolating conductive ways are formed as the CCG flakes overlap.

4.2 Strain sensors

The performance of the CCG stripes as resistive strain sensors was further evaluated by performing uniaxial strain tests. Figure 4.8(a) shows the relative variation of the electrical resistance $(R - R_0) / R_0 = \Delta R / R_0$ of the CCG stripe array as a function of the strain ε applied to the substrate. When fitting the experimental data with an exponential function ($\Delta R / R_0 = e^{g.\varepsilon} - 1$) the sensitivity g is 17, while with a linear fit ($\Delta R / R_0 = g.\varepsilon$) g equals 17.6, the two results being very similar values. The sensitivity g is in good agreement and slightly higher than what was previously observed for graphene-based strain gauges [26]. The sensitivity obtained for the sensors (<200) seems to indicate as dominant the over-connected sheets mechanism in which the sheets lose/gain contact as a result of strain.

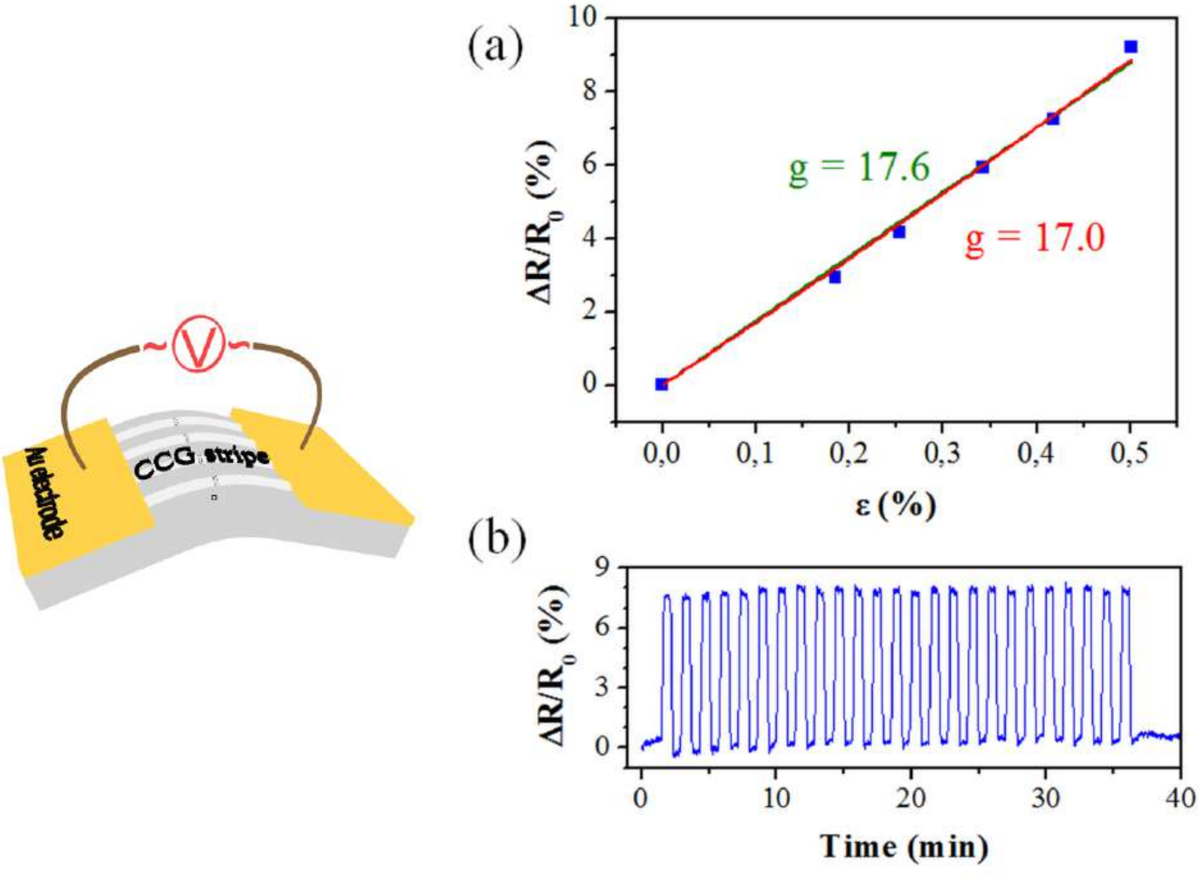

Figure 4.8 – Strain sensor based on CCG stripe: **(a)** Relative variation of the electrical resistance $\Delta R / R_0$ of the CCG-based strain sensor as a function of the strain ε applied to the substrate, with R_0 the electrical resistance at rest; the experimental data is fitted with the equation $\Delta R / R_0 = g.\varepsilon$ with g the gauge factor (green curve) and also with an exponential function $\Delta R / R_0 = e^{g.\varepsilon} - 1$ (red curve); **(b)** Relative variation of the electrical resistance over time $\Delta R / R_0$, while strain values 0.00% and 0.45% are are applied alternatively to the substrate.

Cyclic tests were then performed to characterize the reliability of these sensors (figure 4.8(b)). While CCG-based strain sensors were alternatively stretched up to a strain ε =

0.45%, the amplitude of the electrical resistance variation remained stable. Further, we verified the behaviour of the CCG stripes at higher strains; the samples were stretched up to strains of 2% without breaking, limit imposed by the force limit of our tensile stage. These characterizations proved the high potential of the CCG stripes as resistive strain sensors both in terms of strain sensitivity and repeatability.

4.3 Humidity sensors

We investigate the sensitivity of the CCG stripes to humidity. A quasi linear increase of R_0 of 25% was observed when the RH increases from 10% to 70% (figure 4.9(a)), which is on the same order of magnitude as it was observed on gold nanoparticle based strain gauges [27].

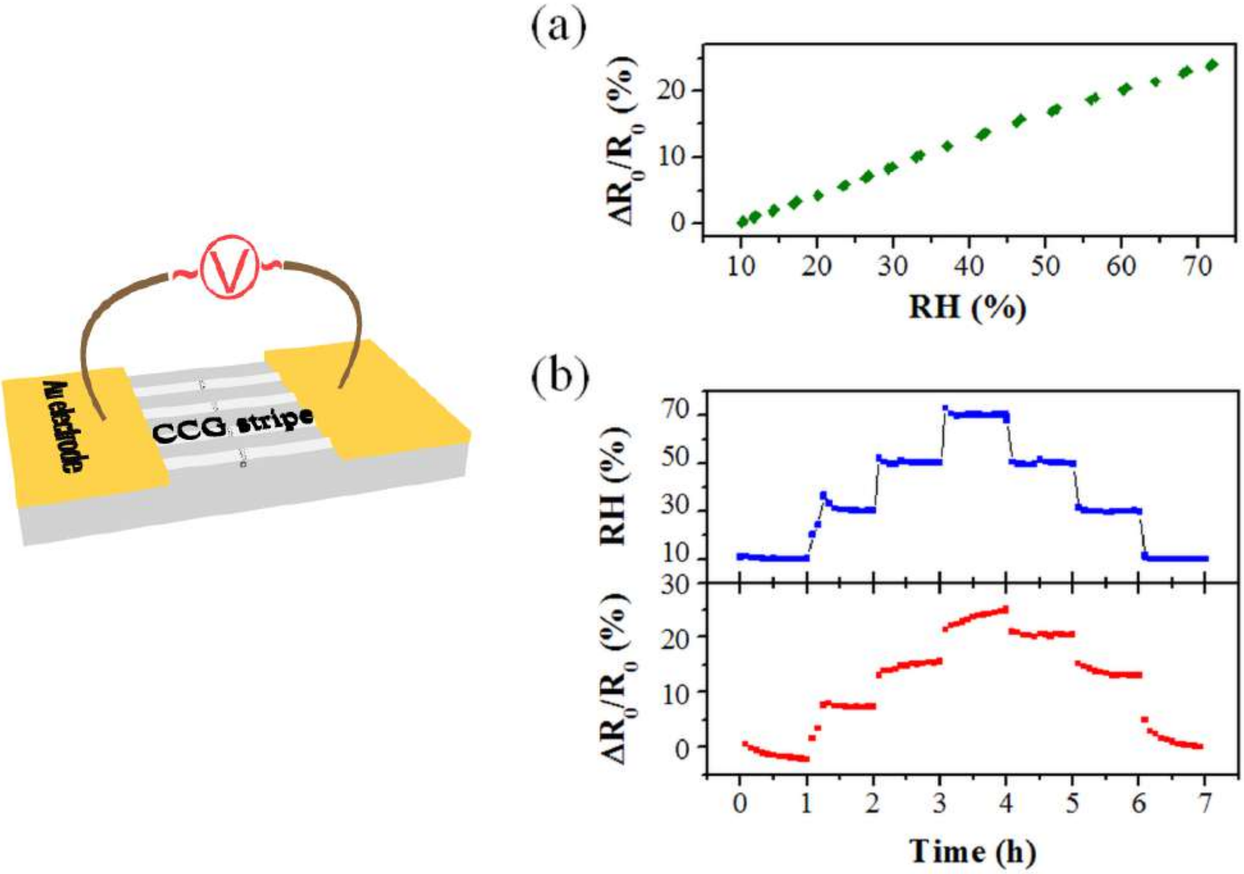

Figure 4.9 – Humidity sensor based on CCG stripe: **(a)** Relative variation of the electrical resistance ΔR_0 / R_0 of CCG stripes at rest (zero strain)as a function of relative humidity (RH) when the RH is increased from 10% to 70% in one step; **(b)** Relative variation of the electrical resistance at rest ΔR_0 / R_0 over time, as a function of RH. R_0 corresponds to the resistance at rest at t = 0h.

In a second experiment, the relative humidity was increased by step of 10% every 60 minutes and then decreased back to 10%. The sensor exhibited the same increase of the electrical resistance at rest of around 25% when the humidity increases from 10 to 70%.

This phenomenon is reversible as the resistance decreased back to its initial value with no hysteresis.

4.4 Illumination induced electrical current enhancement in self-assembled CCG stripes

Another possible technological application of the CCG stripes is in photodetection. In the following we will present some preliminary results regarding the current enhancement inside the CCG stripes assembled on Si/SiO_2 wafers. The schematic representation of the photodetector with CCG stripes as active area is presented below in figure 4.10. LED light at multiple wavelengths is used to illuminate the CCG channel which is under 1V bias.

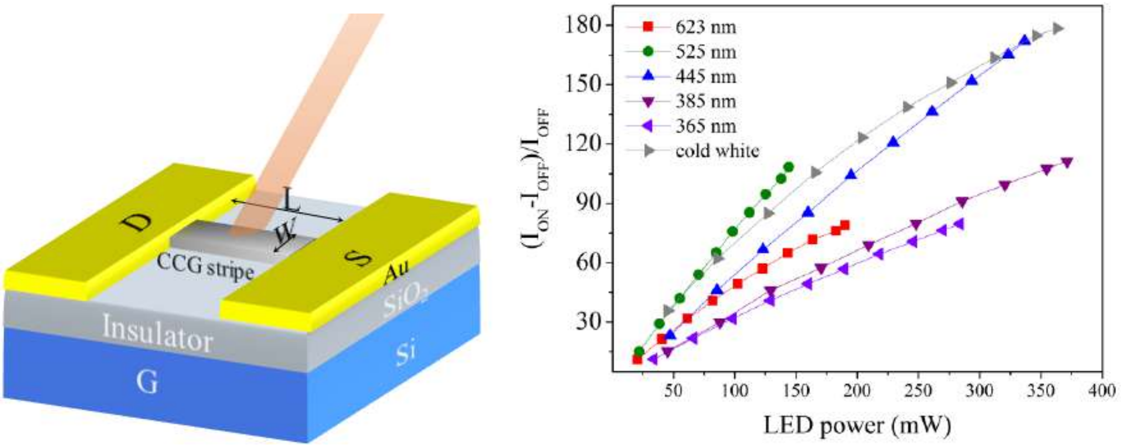

Figure 4.10 – (left) Schematic representation of photodetector with CCG stripe as active area; (right) Current enhancement as function of LED power for different LED wavelengths

At room temperature the electrical current increases as the LED power increases for all the wavelengths investigated (see figure 4.10). The maximum effect, 180 times enhancement, is obtained for white light. Interestingly, the effect is wavelength dependent. The highest increase rate is observed for green LED while the UV light induces the smallest rate. It is not clear yet what is responsible for the enhancement however these results show great promise in terms of obtaining photodetection devices in a cost-effective manner.

Conclusions

- We proposed a facile, low-cost and fast technique to produce patterned CCG films from aqueous dispersions of CCG flakes at extremely low concentrations. The technique also enables the operation at normal pressure and temperature conditions, without any of the presently used lithographic approaches to patterning graphene films.

- Parallel CCG micro-stripes were obtained on rigid and flexible substrates, in a one-step deposition procedure by a modified version of CSA, which allows the stripes' width and spacing to be independently controlled over a wide range of dimensions.

- The as obtained stripes are electrically conductive, with a resistivity three orders of magnitude larger than graphite, highly transparent in the visible-NIR range (>85%) and improved values of electrical mobility of CCG stripes compared to CCG films obtained through other techniques.

- A sensitive strain sensor was developed based on the CCG stripes. The sensitivity is slightly higher than the majority of strain sensors obtained with CVD graphene, and clearly surpasses the conventional metal strain gauges. The sensor is robust, withstanding strains larger than 1% without breaking, the response is stable in time and is reproducible.

- A second electronics application demonstrated in this paper is as humidity sensors. The resistance of CCG stripes exhibited a reversible dependence on humidity, in the range 10-70% RH.

- Preliminary results with LED illumination of the CCG stripes, suggest that they could equally be utilized as active area in photodetection devices.

- The control over stripe density and dimensions, offered by the *Stop&Go* CSA, allows to tune both the transparency and the electrical resistance of CCG stripe arrays. As a perspective, the CCG regular arrays could be obtained on large areas, in multiple morphologies, and in combination with other nanomaterials.

Chapter 5. Revealing the structure and functionality of graphene oxide and reduced graphene oxide/pyrene carboxylic acid interfaces by correlative spectral and imaging analysis

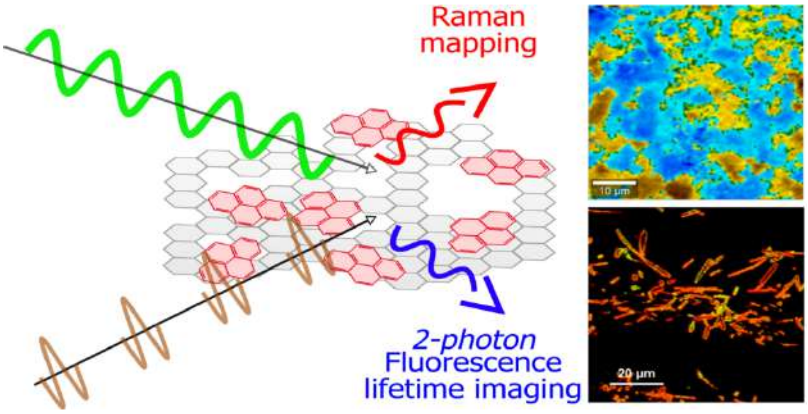

Healing and charge transfer effects in chemically derived graphene interfaces revealed through correlative Raman and two-photon Fluorescence lifetime imaging towards the development of biosensors

The structural uniqueness of graphene, made it necessary to modify its surface with various linkers and functionalities in order to exploit the excellent optical, mechanical and electrical properties that it possesses. Because the focus is on the graphene performance, not so much attention is devoted to understanding the in-depth structural modifications ensueing when the graphene/moiety interface is formed. We report here a high-end effective correlated spectral and imaging multianalysis on two systems: GO and rGO modified with pyrene carboxylic acid (PCA). Confocal Raman mapping was used next to two-photon excited Fluorescence Lifetime Imaging Microscopy (FLIM) to characterize the distribution of PCA on GO and to understand the importance of the inhomogenous distribution of PCA on GO. Preliminary results demonstrating the capacity of the GO-PCA matrix to anchor recognizing moieties via amino-linkage, pave the way for developing biosensors.

5.1 Synthesis of pyrene-carboxylic acid modified graphene oxide (GO-PCA) and reduced graphene oxide (rGO-PCA) interfaces

Pyrene-carboxylic acid (PCA) modified graphene oxide (GO-PCA) nanosheets are formed by simple mixing of PCA with GO at a 4/1 ratio (figure 5.1) in DMF solvent.

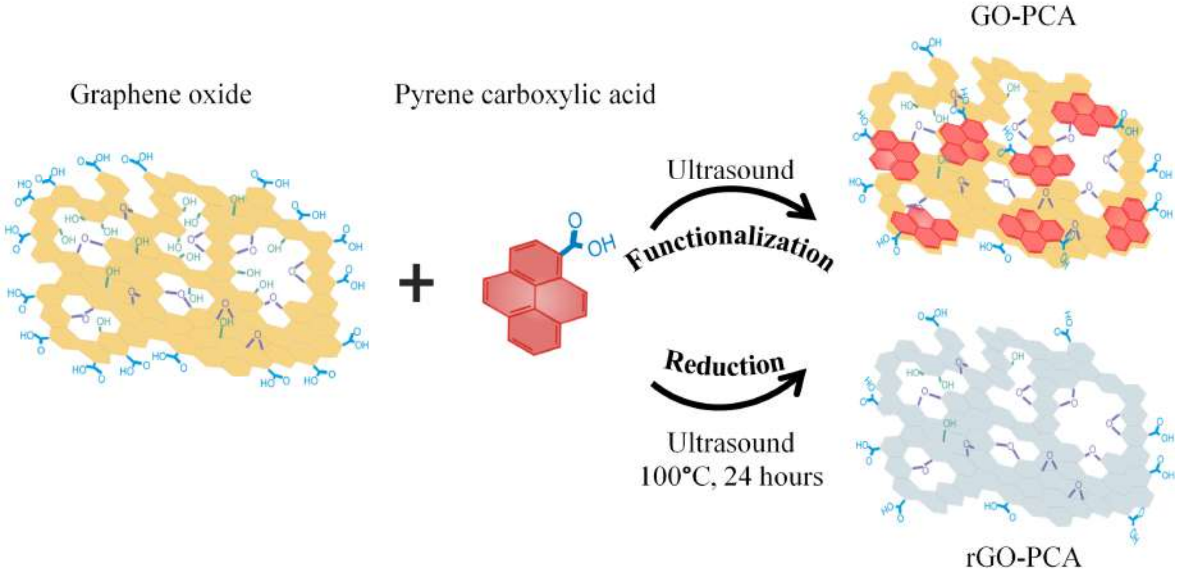

Figure 5.1- Schematic illustration of the functionalization and reduction protocol of graphene oxide with pyrene carboxylic acid molecules.

The large planar aromatic structure of PCA facilitates spontaneous π–π stacking interactions with the graphene network of GO which was favored using sonication. Thus under ultrasounds, using the aromatic core of PCA, the graphene matrix of GO was enriched with carboxyl moieties non-invasively. The reduction of GO to rGO was achieved by heating the GO-PCA mixture for a prolonged time upon which a black precipitate was formed. The resulting GO-PCA and rGO-PCA systems, undergo a correlative spectral and imaging multianalysis to highlight effects occurring at the graphene/moiety interface.

The presence of PCA on the GO nanosheets is validated by the occurrence of several additional absorption bands between 250-450 nm, completely overlapping those of GO (figure 5.2 (a)). After heating, a red shift of the main absorption band to 273 nm and an increase in the absorption tail in the NIR is observed for rGO-PCA, suggesting reduction of the GO nanosheets with the restoration of the electronic conjugation within the GO nanosheets. Our assumption is that the PCA molecules distributed on the GO nanosheets, upon prolonged heating contribute to the restoration of the sp^2 network by fusing into the carbon lattice [28]. The reduction is further confirmed by the the diffractograms recorded on the samples before and after heating (figure 5.2(b)). The line at 2θ higher values is due to (002) plane of the newly formed rGO-PCA and indicates the restoration of the crystalline ordering in of rGO-PCA [29].

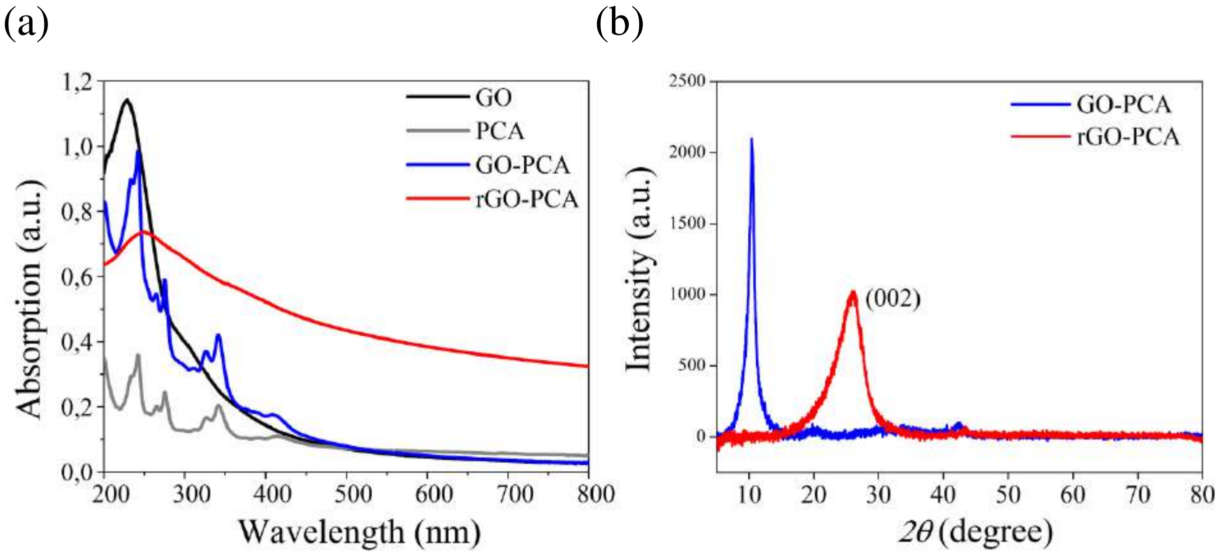

Figure 5.2 - **(a)** UV-vis absorption spectra of GO (black), PCA (grey), GO-PCA (blue) and rGO-PCA (red) in water; **(b)** XRD patterns for GO-PCA and rGO-PCA.

The C_{1s} core level XPS spectra were deconvoluted into four components in good agreement with literature: C-C/C=C bonds in the graphitic lattice [7], C-O bonds in hydroxyl and epoxy groups [7], C=O [7] and carboxyl groups. In the case of GO-PCA, the C-C/C=C component increases and becomes dominant while the contribution of the oxygen-containing groups decreases**.**

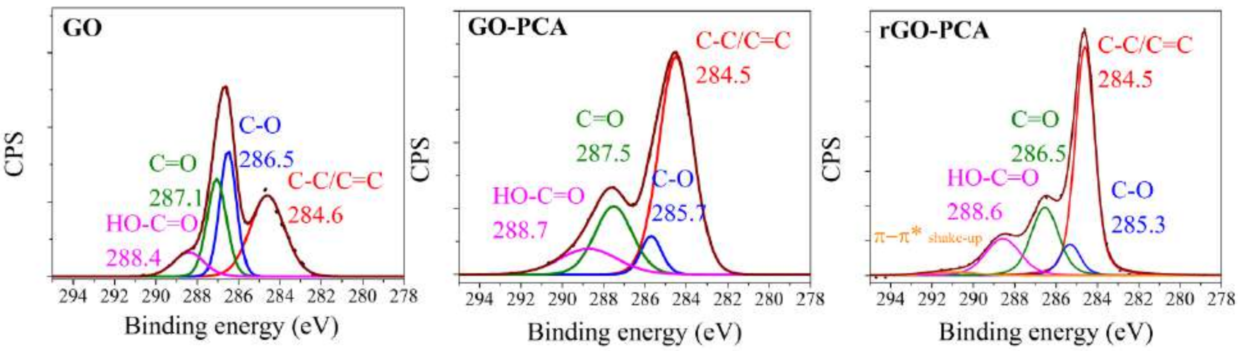

Figure 5.3 - Deconvolution of C_{1s} core level XPS spectra for GO (left), GO-PCA (middle) and rGO-PCA (right) with their corresponding assignments.

Upon heating GO-PCA, the XPS peaks shift to even lower binding energies, the C-C/C=C contribution becomes narrower and a new peak appears, assigned to π-π* shake-up satellite [30]. Such changes would seem to indicate that a restoration of the delocalized π conjugation, typical of aromatic carbon structures, occurred. Notably, the carboxyl functionalities have an enhanced contribution even after the coupling with PCA and heat treatment.

5.2 Investigation of defects and ordering in GO-PCA and rGO-PCA

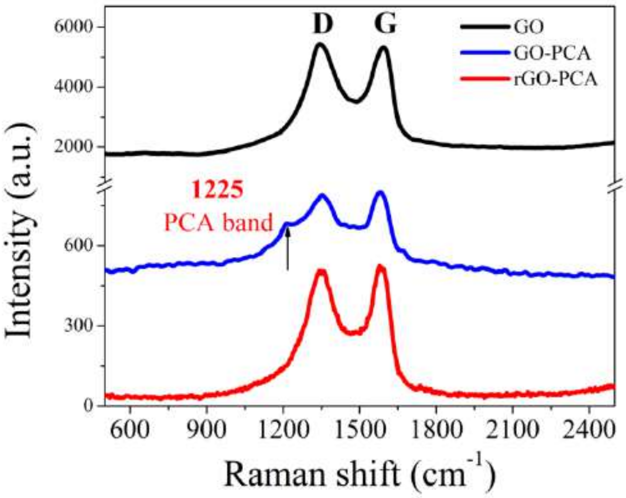

Figure 5.4 - Single point Raman spectra of GO (black), GO-PCA (blue) and rGO-PCA (red) deposited on quartz (Raman excitation: 532 nm).

Spectroscopic analysis

The single point Raman spectra of GO and GO-PCA (figure 5.4(a)) exhibit ***G*** and ***D*** features distinct to carbonaceous structures. In the case of GO-PCA, the ***G*** peak is red shifted by 3 cm^{-1}, while the ***D*** peak broadens. The red shift is consistent with a charge transfer from the PCA to GO which changes the electronic structure of GO by inducing probably *n*-type doping, resulting in softening of the Raman ***G*** peak [31]. Most importantly, a new peak centered at around 1225 cm^{-1} becomes visible. This band is a C-C stretching and C-H bending combined mode of the PCA molecule [32]. In the case of rGO-PCA, the band of PCA is no longer present, confirming the UV-vis findings. However, both ***G*** and ***D*** bands are significantly narrower, which suggests an improved ordering in the structure after heating. For the matrix after heating, the ***G*** peak is shifted even further and, it is associated with the restoration of the graphitic network typical to thermal and chemical reduction.

Raman mapping

Raman mapping was in addition performed for GO-PCA to get a better understanding on the distribution of the PCA molecules on the GO nanosheets (figure 5.5). Raman maps are obtained by integrating the intensity of the G band and the pyrene band at 1225 cm^{-1}. As it can be seen from the merged Raman maps in figure 5.5, GO is not fully covered by PCA, and the PCA molecules rather form clusters on certain sites of GO.

The I_D/I_G ratio band (figure 5.6) map highlights important structural information. The GO-PCA-nanosheets appear to present two types of structural domains: *(i)* one where the I_D/I_G ratio is < 1 and *(ii)* another where this ratio is >1. Comparing figure 5.5 and figure 5.6 one sees clearly that these different domains correspond to GO-PCA and unmodified GO domains. The I_D/I_G decrease in GO-PCA compared to GO (I_D/I_G>1) indicates that the sp^2

domains grow as a result of PCA integration onto GO. PCA acts like a “patch” on the defects and vacancies formed due to the removal of oxygen atoms, as indicated by the XPS analysis.

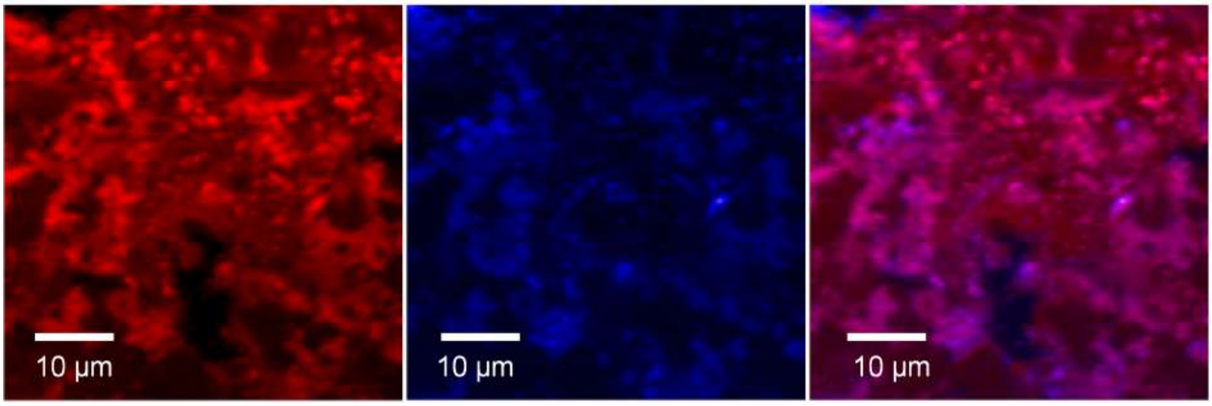

Figure 5.5 - Raman maps of GO-PCA by integrating I_G (left), pyrene band at I_{1225} (center) and merged map (right).

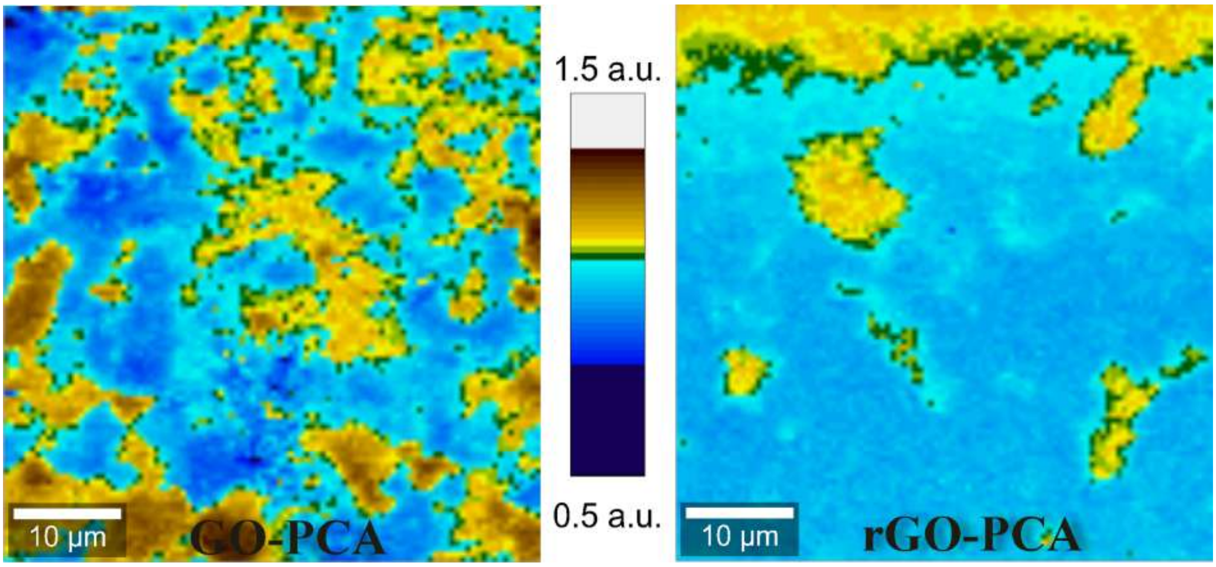

Figure 5.6 - Raman maps of GO-PCA (left) and rGO-PCA (right) by representing I_D/I_G ratio.

After heating, the larger sp^2 domains are more extensive and uniform and the I_D/I_G decreases in the GO domains. As reported in other works [33], the I_D/I_G ratio increases after GO reduction due to the point defects and vacancies that remain in the graphene lattice even after oxygen atoms removal [21]. In the case of rGO-PCA, the I_D/I_G ratio decrease compared to GO, after heating, seems to indicate a “healing” of the sp^2 carbon network. We assume that the PCA molecules coupled to GO fuse into the rGO lattice to form larger sp^2 domains, attesting for the absence of the signature bands of PCA in the UV-vis and the Raman spectra.

Fluorescence lifetime measurements (FLIM)

The charge transfer occurring between the PCA molecules and GO should be clearly distinguishable in FLIM. Graphene and GO are known as good fluorescence quenchers in various chromophore/graphene systems [34] and they are expected to induce a decrease in the fluorescence lifetime of the chromophore. Unlike most reported works, we employ two-photon excitation as it bypasses the increased scattering of the excitation occurring when probing molecules that absorb in the UV region [35], such as pyrene [36]. Under two-photon excitation at 770 nm the GO-PCA system studied here, shows two lifetime components, a short lived one at 0.143 ns emission and a longer component at 10.82 ns results similar to free PCA as reported in the literature [37].

Table 5.1: Fluorescence decay parameters of PCA, GO, GO-PCA and rGO-PCA.

	τ_1 / ns	A_1 (%)	τ_2 / ns	A_2 (%)	χ^2
PCA[37]	2	-	14.80	-	1.25
GO	0.0163	100	-	-	2.06
GO-PCA	0.143	12.6	10.82	87.4	0.95
rGO-PCA	0.014	95.7	0.237	4.3	1.104

τ_n and A_n is lifetime and amplitude of the n^th^ component respectively; χ^2 - indicates the goodness of the fit (1 show a perfect fit).

According to studies performed in liquid and solid state at different pressures, the pyrene excimer (excited dimer) emission typically has a shorter lifetime than the monomer's [38]. We assigned the longer lifetime to the monomer and the shorter lifetime to the combination of the two dimeric species based on the additional steady state fluorescence spectra showing three species as reported previously [39]. Both the monomer and excimer emission typically appear at larger lifetime values [38] than the ones reported here, which we attributed to the interaction of PCA with GO. As expected after the Raman measurements evidencing n-doping of GO after coupling with PCA, the fluorescence lifetime of the PCA molecule decreases due to a charge transfer from the PCA to the GO lattice. These studies point towards a non-uniform PCA distribution on GO, as both excimer and monomer emissions occur. FLIM images support this idea as well; the fluorescence lifetime varies among the probed sample regions (figure 5.7). Furthermore, the rGO-PCA matrix, exhibits extremely short lifetimes and decreased intensity similar to initial GO (figure 5.7) and the typical emission of PCA is no longer present probably as the PCA core becomes fused into GO.

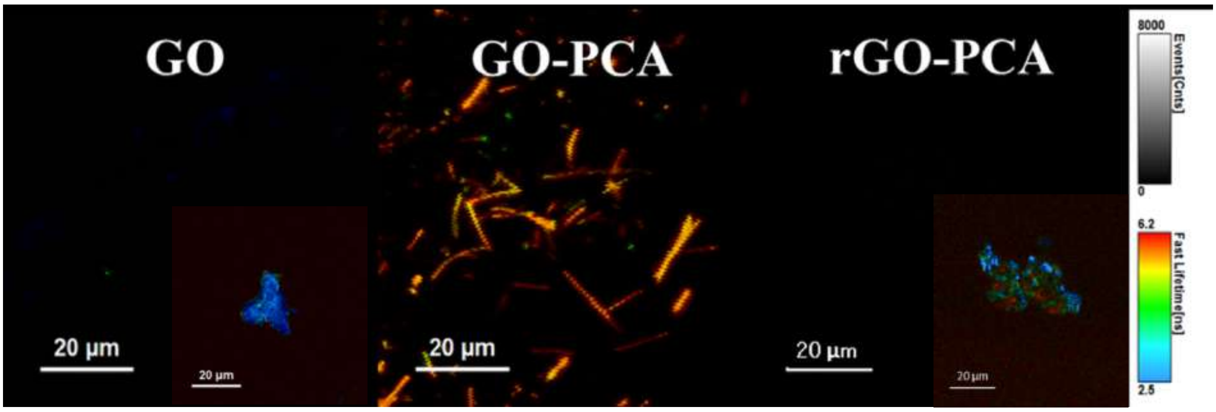

Figure 5.7 - FLIM images of GO (left), GO-PCA (middle) and rGO-PCA (right) obtained under two-photon excitation at 770 nm. The images are represented on identical lifetime scales; the insets represent the FLIM images at a different intensity scale and identical color scale, to visualize the lower emission of GO and rGO-PCA.

5.3 Perspectives. Towards biosensor development

Both systems, GO-PCA and rGO-PCA could be utilized as supporting platforms or active areas components of biosensors. However, because of the undisrupted PCA core on the GO matrix, in the following we focus on the GO-PCA interface and show an optical approach for developing sensors.

GO-PCA interface for sensing

We demonstrate further the adaptability of the GO-PCA interface as a platform to link biorecognizing moieties with a view to sensing and we have chosen to immobilize a lysozyme aptamer. By direct covalent bonding, the -NH_2 terminated aptamer is anchored on the GO-PCA interface via an amide bond formed between the carboxyl groups of the PCA and the amine groups of the aptamer using EDC-NHS chemistry (figure 5.8). The same protocol is performed on control samples using Au coated with unmodified GO, where the native carboxyl groups are the binding sites. SPR angle resolved measurements (figure 5.8) confirm the successful coating of Au interfaces with GO-PCA and GO and further functionalization of these surfaces with lysozyme aptamer by covalent immobilisation. Upon anchoring of the aptamer, the SPR response shifts to higher angles, which is consistent with a higher coverage of the interface. However, the attachment strategy appears to be more effective for the GO-PCA interface, as there is a simultaneous broadening of the dip together with the angle shift. Moreover, the angle is shifted further compared to the direct covalent bonding on GO-covered interface values similar to those reported for physical adsorption of aptamers on graphene-coated SPR interfaces [40].

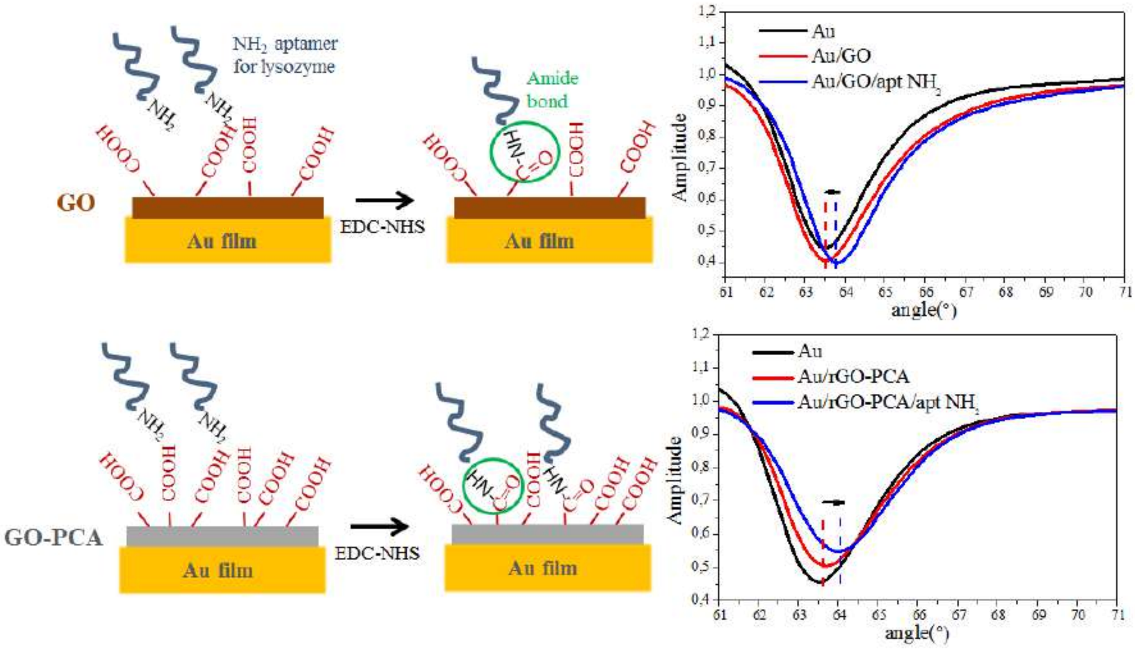

Figure 5.8 –Schematic representation of aptamer attachement protocol by direct covalent binding and angle resolved SPR curves before and after NH_2- aptamer immobilization for GO (top row) and GO-PCA (bottom row).

Conclusions

- High-end spectral and imaging techniques (Raman and two-photon excited FLIM) are employed to extract interface related effects on GO modified with PCA molecules *via* π-π stacking interactions, as well as a GO-PCA matrix heated to form rGO-PCA.
- We are able to visualize the molecular distribution of the PCA distribution on the GO lattice and demonstrate that it is non-homogenous which makes the resulting interface a hybrid structure, presenting sp^2 bonding domains improved and enriched with carboxyl groups due to PCA molecules present, and GO domains where the PCA molecules are not present.
- An n-doping of the underlying GO matrix in the GO-PCA is validated by Raman spectroscopy and FLIM.
- Heating induces further reduction and restoration of the sp^2 bonding beyond the structural domains observed in GO-PCA. The most likely cause is that the aromatic core of PCA molecules becomes fused into the rGO nanosheets while enriching the resulting rGO nanosheets with carboxyl functionalities.
- As perspective research avenues, we show the potential of GO-PCA to anchor biorecognizing moieties with a view to optical sensing.

Chapter 6. Final conclusions and perspectives

I. **We explored and validated two methods for the synthesis of graphene flakes dispersed in liquid phase**

   a. Plasma assisted synthesis starting from chromophore solutions leads to the formation of a variety of carbon structures in terms of morphology mostly amorphous in nature. The synthesis occurs in ambient conditions however is inefficient in producing graphene within the tested experimental conditions.

   b. The top-down production of chemically converted graphene by synthesizing graphite oxide proves to be a cost-effective and sustainable. We thus produced graphene oxide separated according to lateral size and chemically converted graphene readily available for further processing into films required into the practical applications.

II. **We employed convective self-assembly techniques for the fabrication of GO/CCG films**

   a. CSA is a simple and low-cost technique for the production of CCG and GO patterned films (parallel arrays of stripes, grids) and continuous films on a variety of rigid (glass slide, silicon wafers) and flexible substrates (polyethylene terephthalate, polyimide foils).

   b. The geometry of the stripes (width and spacing) can be controlled independently.

   c. Ambient conditions of pressure and temperature are required for the operation of the CSA set-up.

   d. The technique uses record concentrations of CCG flakes (as low as 0.05 mg ml^{-1}) minimizing the material loss.

III. **The CCG patterned films were harnessed into low-cost workable transparent flexible electronic devices for strain and humidity sensing**

   a. Resistive strain sensors were designed based on CCG stripes on PET in a two terminal configuration with the stripes connecting two gold electrodes.

   b. The sensors are robust, show reproducible and reliable response with sensitivity surpassing the conventional metal sensors.

c. Humidity sensors with good sensitivity and reversible response and were developed using the same configuration.
d. The multivalent sensors are flexible and transparent and can be easily incorporated into larger electronic devices.

IV. The structure and functionality of the GO/rGO interfaces with pyrene carboxylic acid were investigated with correlative Raman and two-photon Fluorescence lifetime imaging

a. We synthesized GO-PCA and rGO-PCA interfaces without additional reagents.
b. Raman and FLIM imaging analysis demonstrate the non-homogeneous distribution of the PCA molecules on the GO lattice which affects the structure of GO by producing domains with different I_D/I_G ratios.
c. rGO-PCA displays improved sp^2-conjugation presumably as a result of PCA core fusing into the starting GO matrix leading to a healed rGO but enhanced carboxyl functionalities.
d. GO-PCA is an efficient platform for the anchoring of aptamers for lysozyme via amino-linkage either by direct covalent bonding or by biotin-avidin specific interaction.

V. Perspectives

a. Investigate the mechanism behind the electrical current enhancement inside CCG stripes induced by illumination particularly the role of the stripe/substrate coupling and develop transparent/flexible low-cost photodetectors.
b. Explore further the detection of lysozyme on GO-PCA/rGO-PCA by Surface Plasmon Resonance and develop low-cost sensors.

References

[1] K.S. Novoselov, Electric Field Effect in Atomically Thin Carbon Films, Science. 306 (2004) 666–669.
[2] A. Zurutuza, C. Marinelli, Challenges and opportunities in graphene commercialization, Nat. Nanotechnol. 9 (2014) 730–734.
[3] M. Peplow, Graphene booms in factories but lacks a killer app, Nature. 522 (2015) 268–269.
[4] J.-H. Ahn, B.H. Hong, Graphene for displays that bend, Nat. Nanotechnol. 9 (2014) 737–738.
[5] F.H.L. Koppens, T. Mueller, P. Avouris, A.C. Ferrari, M.S. Vitiello, M. Polini, Photodetectors based on graphene, other two-dimensional materials and hybrid systems, Nat. Nanotechnol. 9 (2014) 780–793.
[6] N. Li, Z. Chen, W. Ren, F. Li, H.-M. Cheng, Flexible graphene-based lithium ion batteries with ultrafast charge and discharge rates, Proc. Natl. Acad. Sci. 109 (2012) 17360–17365.

[7] Z. Bo, X. Shuai, S. Mao, H. Yang, J. Qian, J. Chen, J. Yan, K. Cen, Green preparation of reduced graphene oxide for sensing and energy storage applications, Sci. Rep. 4 (2014).
[8] W. Ren, H.-M. Cheng, The global growth of graphene, Nat. Nanotechnol. 9 (2014) 726–730.
[9] I.W. Frank, D.M. Tanenbaum, A.M. van der Zande, P.L. McEuen, Mechanical properties of suspended graphene sheets, J. Vac. Sci. Technol. B Microelectron. Nanometer Struct. 25 (2007) 2558.
[10] K.F. Mak, L. Ju, F. Wang, T.F. Heinz, Optical spectroscopy of graphene: From the far infrared to the ultraviolet, Solid State Commun. 152 (2012) 1341–1349.
[11] P. Avouris, C. Dimitrakopoulos, Graphene: synthesis and applications, Mater. Today. 15 (2012) 86–97.
[12] E.P. Randviir, D.A.C. Brownson, C.E. Banks, A decade of graphene research: production, applications and outlook, Mater. Today. 17 (2014) 426–432.
[13] K.S. Novoselov, V.I. Fal′ko, L. Colombo, P.R. Gellert, M.G. Schwab, K. Kim, A roadmap for graphene, Nature. 490 (2012) 192–200.
[14] R. Beams, L. Gustavo Cançado, L. Novotny, Raman characterization of defects and dopants in graphene, J. Phys. Condens. Matter. 27 (2015) 083002.
[15] H. Tian, Y. Shu, Y.-L. Cui, W.-T. Mi, Y. Yang, D. Xie, T.-L. Ren, Scalable fabrication of high-performance and flexible graphene strain sensors, Nanoscale. 6 (2014) 699–705. doi:10.1039/C3NR04521H.
[16] Y. Lee, S. Bae, H. Jang, S. Jang, S.-E. Zhu, S.H. Sim, Y.I. Song, B.H. Hong, J.-H. Ahn, Wafer-Scale Synthesis and Transfer of Graphene Films, Nano Lett. 10 (2010) 490–493.
[17] H. Bi, K. Yin, X. Xie, J. Ji, S. Wan, L. Sun, M. Terrones, M.S. Dresselhaus, Ultrahigh humidity sensitivity of graphene oxide, Sci. Rep. 3 (2013). doi:10.1038/srep02714.
[18] W.S. Hummers, R.E. Offeman, Preparation of Graphitic Oxide, J. Am. Chem. Soc. 80 (1958) 1339–1339.
[19] M. Iliut, A.-M. Gabudean, C. Leordean, T. Simon, C.-M. Teodorescu, S. Astilean, Riboflavin enhanced fluorescence of highly reduced graphene oxide, Chem. Phys. Lett. 586 (2013) 127–131.
[20] S. Saxena, T.A. Tyson, S. Shukla, E. Negusse, H. Chen, J. Bai, Investigation of structural and electronic properties of graphene oxide, Appl. Phys. Lett. 99 (2011) 013104. doi:10.1063/1.3607305.
[21] C. Gómez-Navarro, R.T. Weitz, A.M. Bittner, M. Scolari, A. Mews, M. Burghard, K. Kern, Electronic Transport Properties of Individual Chemically Reduced Graphene Oxide Sheets, Nano Lett. 7 (2007) 3499–3503.
[22] C.J. Shearer, A.D. Slattery, A.J. Stapleton, J.G. Shapter, C.T. Gibson, Accurate thickness measurement of graphene, Nanotechnology. 27 (2016) 125704. doi:10.1088/0957-4484/27/12/125704.
[23] Z. Ni, Y. Wang, T. Yu, Z. Shen, Raman spectroscopy and imaging of graphene, Nano Res. 1 (2008) 273–291.
[24] C. Farcau, N.M. Sangeetha, H. Moreira, B. Viallet, J. Grisolia, D. Ciuculescu-Pradines, L. Ressier, High-Sensitivity Strain Gauge Based on a Single Wire of Gold Nanoparticles Fabricated by Stop-and-Go Convective Self-Assembly, ACS Nano. 5 (2011) 7137–7143.
[25] Y. Mino, S. Watanabe, M.T. Miyahara, Fabrication of Colloidal Grid Network by Two-Step Convective Self-Assembly, Langmuir. 27 (2011) 5290–5295.
[26] J. Zhao, C. He, R. Yang, Z. Shi, M. Cheng, W. Yang, G. Xie, D. Wang, D. Shi, G. Zhang, Ultra-sensitive strain sensors based on piezoresistive nanographene films, Appl. Phys. Lett. 101 (2012) 063112.
[27] L. Digianantonio, M. Gauvin, T. Alnasser, D. Babonneau, B. Viallet, J. Grisolia, G. Viau, A. Coati, Y. Garreau, L. Ressier, Influence of the Humidity on Nanoparticle-Based Resistive Strain Gauges, J. Phys. Chem. C. (2016).
[28] X. Wang, L. Zhi, N. Tsao, Ž. Tomović, J. Li, K. Müllen, Transparent Carbon Films as Electrodes in Organic Solar Cells, Angew. Chem. Int. Ed. 47 (2008) 2990–2992. doi:10.1002/anie.200704909.
[29] L. Tang, Y. Wang, Y. Li, H. Feng, J. Lu, J. Li, Preparation, Structure, and Electrochemical Properties of Reduced Graphene Sheet Films, Adv. Funct. Mater. 19 (2009) 2782–2789. doi:10.1002/adfm.200900377.
[30] A. Ganguly, S. Sharma, P. Papakonstantinou, J. Hamilton, Probing the Thermal Deoxygenation of Graphene Oxide Using High-Resolution In Situ X-ray-Based Spectroscopies, J. Phys. Chem. C. 115 (2011) 17009–17019.
[31] B. Das, R. Voggu, C.S. Rout, C.N.R. Rao, Changes in the electronic structure and properties of graphene induced by molecular charge-transfer, Chem. Commun. (2008) 5155.
[32] M. Karabacak, M. Cinar, M. Kurt, P. Chinna babu, N. Sundaraganesan, Experimental and theoretical FTIR and FT-Raman spectroscopic analysis of 1-pyrenecarboxylic acid, Spectrochim. Acta. A. Mol. Biomol. Spectrosc. 114 (2013) 509–519.
[33] C. Gómez-Navarro, R.T. Weitz, A.M. Bittner, M. Scolari, A. Mews, M. Burghard, K. Kern, Electronic Transport Properties of Individual Chemically Reduced Graphene Oxide Sheets, Nano Lett. 7 (2007) 3499–3503.
[34] H.-J. Kim, J. Sung, H. Chung, Y.J. Choi, D.Y. Kim, D. Kim, Covalently Functionalized Graphene Composites: Mechanistic Study of Interfacial Fluorescence Quenching and Recovery Processes, J. Phys. Chem. C. 119 (2015) 11327–11336.
[35] R.K.P. Benninger, D.W. Piston, Two-Photon Excitation Microscopy for the Study of Living Cells and Tissues, in: J.S. Bonifacino, M. Dasso, J.B. Harford, J. Lippincott-Schwartz, K.M. Yamada (Eds.), Curr. Protoc. Cell Biol., John Wiley & Sons, Inc., Hoboken, NJ, USA, 2013.
[36] X.-T. Liu, Y. Zhao, A.-M. Ren, J.-K. Feng, A comparative study of one- and two-photon absorption properties of pyrene and perylene diimide derivatives, J. Mol. Model. 17 (2011) 1413–1425.
[37] J.C. Hicks, R. Dabestani, A.C. Buchanan, C.W. Jones, Spacing and Site Isolation of Amine Groups in 3-Aminopropyl-Grafted Silica Materials: The Role of Protecting Groups, Chem. Mater. 18 (2006) 5022–5032.
[38] P. Conlon, C.J. Yang, Y. Wu, Y. Chen, K. Martinez, Y. Kim, N. Stevens, A.A. Marti, S. Jockusch, N.J. Turro, W. Tan, Pyrene Excimer Signaling Molecular Beacons for Probing Nucleic Acids, J. Am. Chem. Soc. 130 (2008) 336–342.
[39] F. Ito, T. Kakiuchi, T. Sakano, T. Nagamura, Fluorescence properties of pyrene derivative aggregates formed in polymer matrix depending on concentration, Phys. Chem. Chem. Phys. 12 (2010) 10923.

[40] P. Subramanian, A. Lesniewski, I. Kaminska, A. Vlandas, A. Vasilescu, J. Niedziolka-Jonsson, E. Pichonat, H. Happy, R. Boukherroub, S. Szunerits, Lysozyme detection on aptamer functionalized graphene-coated SPR interfaces, Biosens. Bioelectron. 50 (2013) 239–243.

List of publications

Publications related to the thesis

D. Zaharie-Butucel, M. Potara, A. M. Craciun, R. Boukherroub, S. Szunerits, and S. Astilean, *Revealing the structure and functionality of graphene oxide and reduced graphene oxide/pyrene carboxylic acid interfaces by correlative spectral and imaging analysis*, Physical Chemistry Chemical Physics (**IF-4.123, AIS-1.123**), **19**, 16038–16046, 2017.

D. Zaharie-Butucel, L. Digianantonio, C. Leordean, L. Ressier, C. Farcau, S. Astilean, *Flexible transparent sensors with reduced graphene oxide micro-stripes fabricated by convective self-assembly*, Carbon (**IF-6.337, AIS-1.368**), **113**, 361–370, 2017.

D. Zaharie-Butucel, J. Papp, C. Leordean and S. D. Anghel, *Differently ordered carbonaceous structures synthesized by bubbled Ar or He plasmas inside methylene blue solutions with contrasting Escherichia coli growth inhibition effects,* RSC Advances (**IF-3.108, AIS-0.589**), **5**, 98325-98334, 2015.

Other ISI publications

S.D. Anghel, **D.Zaharie-Butucel** and I.E. Vlad, *Single electrode Ar bubbled plasma source for methylene blue degradation and concurrent synthesis of carbon based nanoparticles*, Journal of Electrostatics, 75, 63–71, 2015

D. Zaharie-Butucel and S.D.Anghel, *Optical characterization and application of an atmospheric pressure Ar plasma in contact with liquids for organic dyes degradation*, Rom. Journ. Phys., 59(7), 757-766, 2014